Multiferroic Sensing-Logic Photodetectors for Encryption Communication

Xiaoming Wang(王晓敏)†, Wenlong Su(苏文龙)†, Li Zhen(甄理), Chunyan He(何春艳), Shifeng Zhao(赵世峰)*, and Yulong Bai(白玉龙)*

School of Physical Science and Technology, & Inner Mongolia Key Laboratory of Microscale Physics and Atomic Manufacturing, Inner Mongolia University, Hohhot 010021, China

(Received 22 January 2026; accepted manuscript online 8 April 2026)

Near-sensor computing technology shows high efficiency and intelligence, exhibiting significant promise in the post-Moore era. The light power density and wavelength are used as the stimulations to implement reconfigurable logic operations (AND, OR) in dual-band-response $Bi_{0.5}Na_{0.5}Ti_{0.85}Fe_{0.15}O_3$ multiferroic photodetectors, where the polarization-dependent photocurrents are the weighting factors. The p–d hybridization between the O atom and Fe dopants constructs the mixed band structure and carrier transport network. The in-sensor computing photodetectors showcase optical encryption communication of the English alphabet and Chinese characters by ASCII code. This research holds promise for the in-sensor computing paradigm, enabling complex tasks.

DOI: 10.1088/0256-307X/43/5/050802 CSTR: 32039.14.0256-307X.43.5.050802

The in-sensor computing photodetectors are significant for artificial intelligence and cloud computing.[1] The traditional photodetectors possess only sensing functionality and are susceptible to information leakage, whereas broad-spectrum photodetectors suffer from signal crosstalk due to simultaneous response to multiple wavelength ranges.[2] Based on dual-band photodetectors, unauthorized users lack knowledge of the correct modulation wavelength or modulation scheme; thus, the transmitted information cannot be accurately decoded, which enhances communication security.[3] Conventional strategies, such as physically connecting multiple single-band photodetectors or constructing complex heterostructures, often lead to increased complexity, high energy consumption, limited operational lifetime, and poor scalability.[4] Moreover, additional sophisticated circuits are required to perform information processing. The physical separation between sensing and computing is highly unfavorable for efficient data processing and energy conservation. The composition and dopant-assisted electronic states of ferroelectrics can greatly tailor the band structure and polarization, enabling multi-band photodetection and logic operations.[5] Thus, self-powered ferroelectric photodetectors exhibit potential for dual-band response and logic operations.[6]

In recent years, most reported near-sensor computing technologies are based on various heterojunctions, which are subject to complex fabrication processes, interface defects, and dopant diffusion.[7] The ferroelectric photodetectors combine photoresponse with programmable logic operations, where encoded/decoded encryption communication is implemented using wavelength, optical power intensity, and polarization states.[8] Judicious modulation of oxygen vacancies extends the absorption capability of ferroelectric oxides, and ultra-broadband absorption, from the ultraviolet to the mid-infrared range, is achieved in tetragonal tungsten-bronze structures.[9] Compared with ferroelectric photodetectors, multiferroic-based photodetectors offer multi-state programmability and multifunctional integration within a single device.[10,11] An additional degree of freedom for regulating photon absorption and carrier transport arises from ferromagnetic domain walls.[12] Multiferroics have emerged as promising candidates owing to their internal charge transport networks and strong correlation between photocurrent and magnetic order.[13] In this work, multiferroic ceramics $Bi_{0.5}Na_{0.5}Ti_{1-x}Fe_xO_3$ (x = 0, 0.05, 0.1, 0.15, 0.2, and 0.25) are designed; the raw materials and synthesis conditions are provided in the Supplementary Materials (SM). Aliovalent Fe ionic substitution is employed to introduce oxygen vacancies and magnetic ordering. Both oxygen vacancies and Fe dopants play critical roles in tailoring the electronic structure, enabling dual-band response, and constructing the photocarrier transport pathway. A schematic diagram of the ceramic photodetectors is presented in Fig. S1 of the SM. Ferroelectric properties were measured using a Radiant Technologies Multiferroic 500 system in a silicone oil bath, with pre-polarization applied via a high-voltage source (10 kV). The elapsed time of voltage application (0 → 1 kV) is approximately 2 minutes, followed by holding at 1 kV for 0.5 h. Temperature-dependent permittivity curves were recorded using an Agilent E4980A A and a home-built feedback heater (1 ℃/min). The microstructure was presented via secondary electron imaging (Hitachi Regulus 8100). Optical reflectance and photoluminescence spectra were acquired using the Hitachi UV-4800 and F-7000, respectively. Dynamic photocurrent responses were measured using a high precision meters (Keysight 2450) and LabVIEW software. The tunable

†These authors contributed equally to this work.

*Corresponding authors. Email: zhsf@imu.edu.cn; ylbai@imu.edu.cn

© 2026 Chinese Physical Society and IOP Publishing Ltd. All rights, including for text and data mining, AI training, and similar technologies, are reserved.

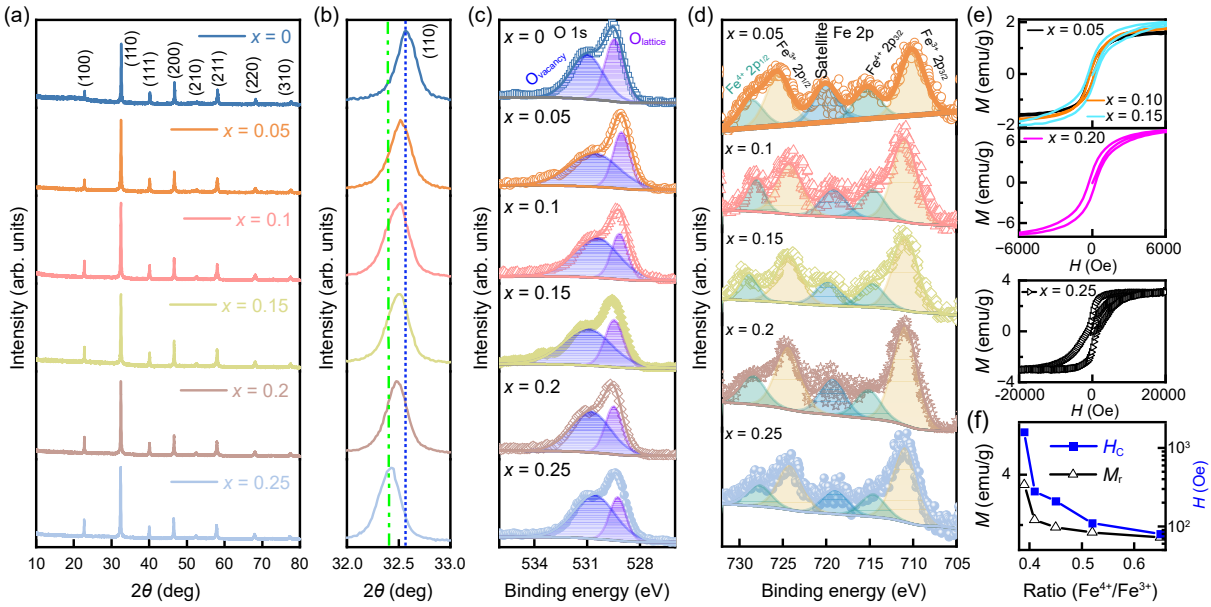

Fig. 1. (a) XRD patterns. (b) Enlarged details. (c) O 1s spectra. (d) Fe 2p spectra. (e) Magnetization hysteresis loops. (f) Dependence of remanent magnetization $M_{\rm r}$ and coercive field $H_{\rm C}$ on the Fe^{4+}/Fe^{3+} ratio.

light source was provided by the 7-SEO instrument (Beijing Saifan Photoelectric Instrument Co., Ltd.).

The phase structure was analyzed using an X-ray diffractometer (PANalytical B.V.), and Rietveld analysis method summarized the parameters in Fig. S2 of the SM, where the unit cell volume $V_{\rm m}$ monotonically increases. No secondary phase is observed, and all the patterns are assigned to the rhombohedral structure with $Pm\bar{3}m$ symmetry in Fig. 1(a).[14] The intensity of the (100) peak increases with the introduction of Fe ions, indicating lattice expansion. Meanwhile, the depression of the (211) peak implies in-plane distortion, and aliovalent Fe doping induces a low-angle shift of the (110) peak in Fig. 1(b). Oxygen vacancies at the doping sites weaken the electron shielding effect, so the nuclear Coulomb repulsion causes the departure of ion cores, promoting lattice expansion.[15] The valence states of O 1s orbital electrons in Fe-doped $Bi_{0.5}Na_{0.5}Ti_{1-x}Fe_xO_3$ ceramics are shown in Fig. 1(c); two distinct peaks appear at binding energies of approximately 531.04 eV and 529.45 eV. The former peak indicates oxygen vacancies, and the latter is contributed by lattice oxygen.[16] The area ratio $O_{\rm lattice}/O_{\rm vacancy}$ decreases with increasing Fe content, from 0.81 ($x = 0.00$) to 0.39 ($x = 0.25$), a trend further confirmed by the normalized intensity method with Bi 4f intensity.[17] Mixed-valence states of Fe are evidenced by the spectra in Fig. 1(d): three peaks at 710.91 eV, 718.33 eV, and 724.69 eV are assigned to Fe^{3+} ($2p_{3/2}$), Fe^{4+} ($2p_{3/2}$), and Fe^{3+} ($2p_{1/2}$), respectively. No significant binding energy shifts are observed for Bi $4f_{7/2}$, Na 1s, and Ti 2p levels in Fig. S3 of the SM. Both Fe and Ti cations adopt 4+ oxidation states; the most plausible electronic structure is the mixture of Fe^{4+} ($t_{2g}^3e_g^1$) and Fe^{3+} ($t_{2g}^3e_g^2$) to compensate for a deficiency of O^{2-} anions.[18] Room-temperature magnetic hysteresis loops are presented in Fig. 1(e), where magnetization correlates with oxygen vacancy density. Positively charged

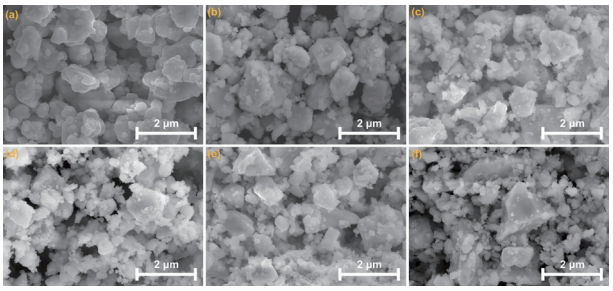

Fig. 2. Microstructure of $Bi_{0.5}Na_{0.5}Ti_{1-x}Fe_xO_3$ ceramics: (a) $x = 0$; (b) $x = 0.05$; (c) $x = 0.1$; (d) $x = 0.15$; (e) $x = 0.2$; (f) $x = 0.25$.

oxygen vacancies act as electron-trapping centers and tend to be energetically in a charge-imbalanced states; the created itinerant electrons overlap with the 3d shell of heterovalent Fe ions, enabling long-range ferromagnetic ordering by F-center exchange coupling.[19] Remanent magnetization $M_{\rm r}$ and coercive field $H_{\rm C}$ are sensitive to the ratio of Fe^{4+}/Fe^{3+} as shown in Fig. 1(f). Tuning charge injection by this ratio demonstrates the control of magnetism in oxygen vacancies: where low-spin d4 coupled with high-spin d5 in a 180° bonding alignment promotes the delocalized superexchange.[20,21]

Magnetic Fe dopants significantly regulate the morphology as shown in Fig. 2, including grain size (shape) and internal connection. For the composition $x = 0$, uniformly coarse grains with smooth grain boundaries are observed in Fig. 2(a). According to the thermodynamic description of solid-state sintering, the curvature-driven force arises from the reduction in total Gibbs free energy.[16] When the surface energy density $\gamma_{\rm S}$ exceeds the grain boundary energy density $\gamma_{\rm GB}$, moderate grain growth favors surface elimination. As the Fe doping concentration increases, grain size gradually becomes finer and more nonuniform size distribution, marked with fine particles at local regions in Figs. 2(b) and 2(c). In light-doping ceramics

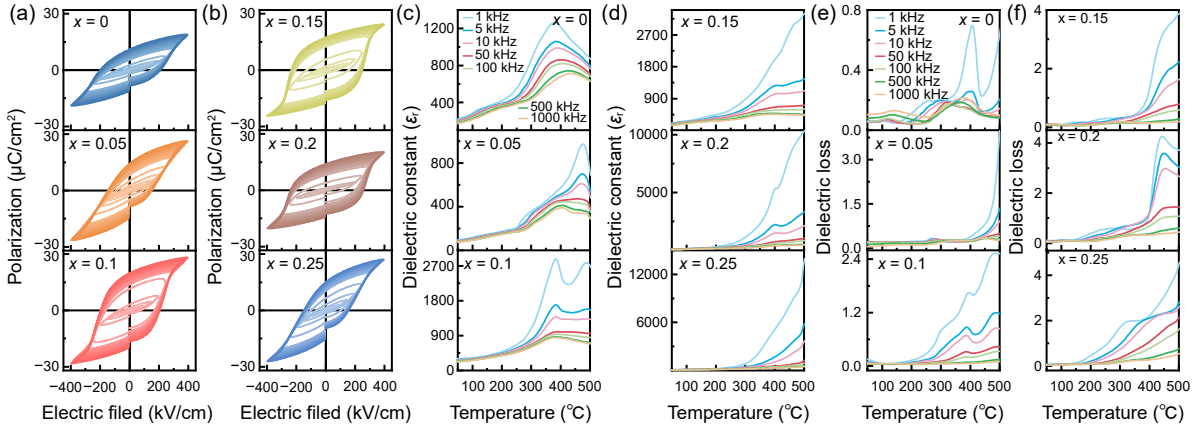

Fig. 3. Ferroelectric performance: (a) $x = 0$, 0.05, 0.1; (b) $x = 0.15$, 0.2, 0.25. Temperature and frequency-dependent dielectric spectra: (c) and (d) relative permittivity; (e) and (f) dielectric loss.

($x = 0.05$ and 0.10), the increment of oxygen vacancies reduces grain boundary mobility by releasing the local grain boundary energy, thereby suppressing local grain growth. The effective chemical potential difference between grain boundaries and surfaces drives curvature change by the relation [22]

$$\mu = \mu_0 + \gamma V_{\mathrm{m}} \frac{2}{r}, \tag{1}$$

where μ is the chemical potential, V_{m} is the cell volume, and r is the effective curvature radius. The increased curvature-driven by chemical potential gradient explains the observed refinement of grains. As the doping concentration increases to $x = 0.15$, the porosity increases significantly with irregular shapes, as shown in Fig. 2(d). Defect accumulation at grain boundaries leads to obvious energy difference between the surface and grain boundary in heavily doped ceramics, which is unfavorable for pore elimination and uniform grain growth, as shown in Fig. 2(e). The coexistence of large block-like grains and surrounding fine grains is observed at $x = 0.25$, indicating microstructural phase separation, as shown in Fig. 2(f). Interfacial energy inhomogeneity likely promotes anisotropic grain growth while simultaneously impeding pore elimination, thereby yielding a complex and non-uniform microstructure. The densification level $p\,(\%)$ and porosity $1 - p$ depend on the doping concentration, as shown in Fig. S4 of the SM, which generally have influence on the ferroelectric polarization.

Ferroelectric polarization of $Bi_{0.5}Na_{0.5}Ti_{1-x}Fe_xO_3$ ($x = 0$, 0.05, 0.1, 0.15, 0.2, and 0.25) ceramic photodetectors is shown in Figs. 3(a) and 3(b). The sharp profile indicates the reliable ferroelectric polarization rather than the leakage current. Polarization current curves in Fig. S5 of the SM validate the robust ferroelectric behavior, where maximum currents near the coercive field confirm the contribution of domain switching. [23] Remanent polarization P_{r} and coercive field E_{C} exhibit strong dependence on the doping concentration. Remanent polarizations of Fe-doped photodetectors exceed those of undoped $Bi_{0.5}Na_{0.5}TiO_3$ photodetectors. At the component $x = 0.15$, the hysteresis loop still retains a well-defined ferroelectric character, and the P_{r} progressively reaches 18.8 $\mu C/cm^2$ in Fig. 3(b). Similar performance is also observed at the component $x = 0.20$; however, the hysteresis loops become slimmer and the remanent polarization decreases markedly in $Bi_{0.5}Na_{0.5}Ti_{0.75}Fe_{0.25}O_3$ photodetectors. Meanwhile, the coercive field exhibits a pronounced non-monotonic dependence on Fe content: it decreases from 216 kV/cm ($x = 0$) to 164 kV/cm ($x = 0.05$), then increases to 218 kV/cm ($x = 0.10$), further rises to 265 kV/cm at $x = 0.15$ and 0.20, and finally drops to 160 kV/cm at $x = 0.25$. Increased acceptor-type defects (Fe^{3+}) and oxygen vacancies are expected to introduce strong local random fields and enhance defect-dipole interactions, which hinder domain-wall motion and completely switching. Furthermore, the disordered distribution of aliovalent Fe induces the formation of local structure inhomogeneity, pore and grain boundary aggregation, which contribute to the relaxor state. [24–26] Consequently, polarization is dominated by short-range polar fluctuations rather than classical ferroelectric domain switching.

The temperature- and frequency-dependent dielectric spectra for $Bi_{0.5}Na_{0.5}Ti_{1-x}Fe_xO_3$ ($x = 0$, 0.05, 0.1, 0.15, 0.2, and 0.25) ceramic photodetectors are discussed in Figs. 3(c) and 3(d). And the ceramic photodetectors ($x = 0.00$, 0.05, 0.10, and 0.15) exhibit peaks at a specific temperature. The peaks are independent of frequency, confirming the ferroelectric–paraelectric phase transition (rhombohedral $Pm\bar{3}m$ to a tetragonal $P4bm$) for $Bi_{0.5}Na_{0.5}TiO_3$ ceramics. The observations of broader transition peak and high transition temperature in Figs. 3(c) and 3(d) show the pronounced frequency dispersion of the relative permittivity in doped ceramics, which is ascribed to the unstable polar structure induced by oxygen vacancies. [27] The emergent peak at 360 ℃ for component $x = 0.05$ and 0.1 is induced by magnetic ordering. Moreover, the dielectric peaks shift toward higher temperatures with increasing frequency, exhibiting typical relaxor character at $x = 0.05$. The magnetic orders in the doped photodetectors can share responsibility of thermal fluctuation, so the ferroelectric phase transition peaks of $Bi_{0.5}Na_{0.5}Ti_{0.85}Fe_{0.15}O_3$, $Bi_{0.5}Na_{0.5}Ti_{0.8}Fe_{0.2}O_3$, and $Bi_{0.5}Na_{0.5}Ti_{0.75}Fe_{0.25}O_3$ photodetectors exceed 600 ℃ in Fig. 3(c). Furthermore, evident frequency dispersion and progressive suppression of the dielectric peaks are

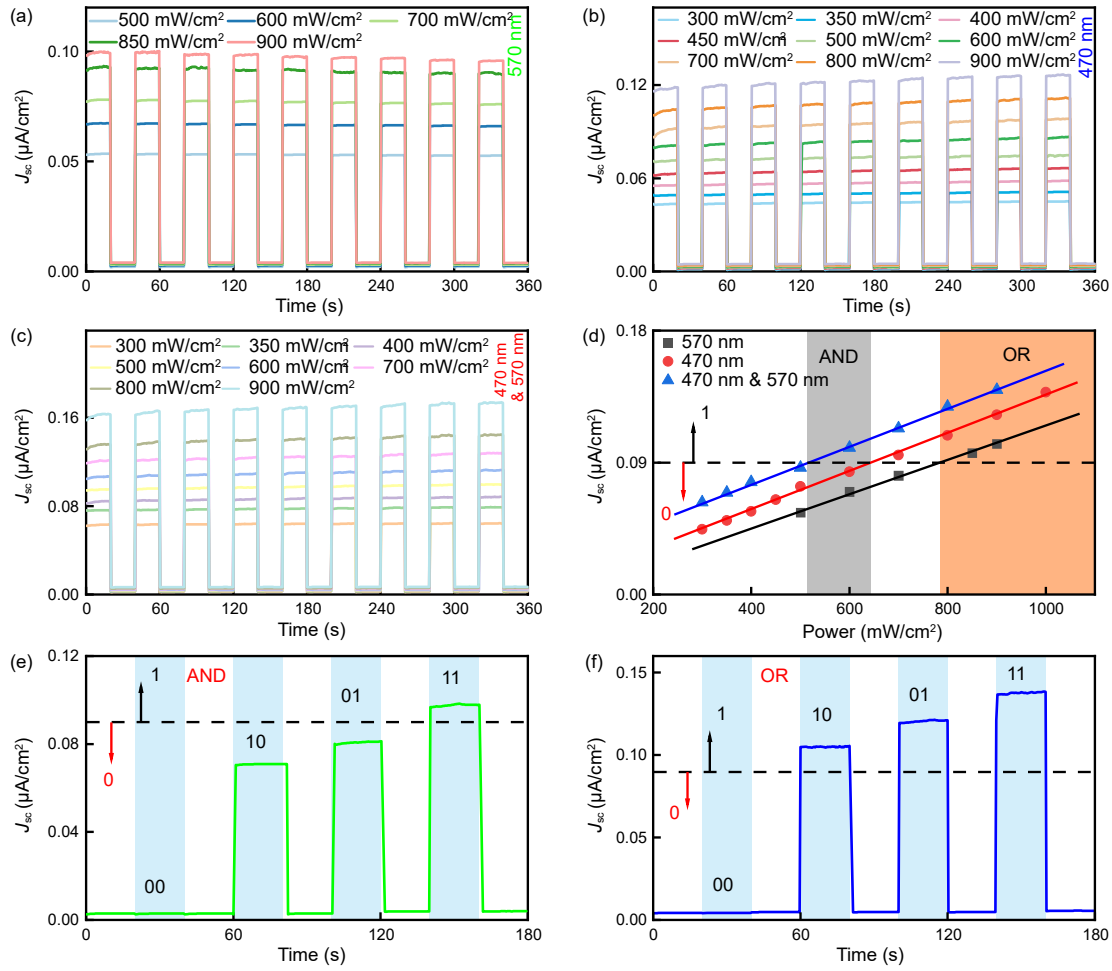

Fig. 4. The switchable photocurrents: (a) 570 nm, (b) 470 nm, (c) 570 nm, and 470 nm. (d) photocurrent versus irradiation power curves. (e) "AND" and (f) "OR" logical operations.

observed in heavily doped photodetectors ($0.15 \leq x \leq 0.25$) in Fig. 3(d). Migratable carriers and defect polarizations induced by heterovalence dopants are inactive under high-frequency electric fields. Consequently, short-range polar fluctuation processes dominate the mixed response which shows both peak broadening and frequency dispersion.[28] A set of dielectric loss peaks is observed in Figs. 3(e) and 3(f), and similar phenomena have been reported in lead zirconate titanate ceramics.[27,29] The dielectric loss exhibits two broad peaks; the lower-temperature peak is attributed to the dielectric relaxation, which progressively diminishes with the increment of Fe content because the domain wall movement is strongly pinned by oxygen vacancies. The aliovalent Fe doping not only distorts the ferroelectric structure but also affects the local charge density. Charged defects can be trapped or accumulated at polar regions, which present large dielectric loss.

The $Bi_{0.5}Na_{0.5}Ti_{1-x}Fe_xO_3$ ($x \geq 0.1$) photodetectors present vivid dual-band absorption at 470 nm and 570 nm, which show polarization-dependent photocurrents in Fig. S6 of the SM. Under illumination, the d-band center of Fe governs the photon absorption, and p-band center of O governs photoelectron emission. Based on the "electron pump" effect of p–d orbital hybridization, the electron hopping mechanism is illustrated in Fig. S7 of the SM, where the Fe-O-Ti bridging structure is proposed to elaborate the dual-band response. Excitation, separation, and transport are crucial for photocurrent generation. The charged oxygen vacancy has a spin-triplet ground state with a spin-dependent optical absorption. The weakly coupled spin pairs involve two point defects, contributing to the emergent photoluminescence (535 nm). The optical absorption-driven electron hopping between the defects corresponds to the absorption (570 nm) in Fig. S6 of the SM.[30] The remarkable increase in photocurrent in Figs. S6(d) and S6(e) is ascribed to the internal transport network by the multiferroic domain walls, as well as the electronic and energy band structure. The coupling between local magnetic moments and the optical absorption process facilitates photon trapping in polycrystalline multiferroics, thereby promoting the formation, excitation, and separation of relatively long-lived spin-1/2 electron–hole pairs.[31] The $Bi_{0.5}Na_{0.5}Ti_{0.85}Fe_{0.15}O_3$ photodetectors exhibit a compelling photocurrent compared with other components in Fig. S6 of the SM. The $Bi_{0.5}Na_{0.5}Ti_{0.85}Fe_{0.15}O_3$ photodetectors show a dual-band photoresponse, with rise/decay times of 250 ms in Fig. S8 of the SM. Figure 4(a) presents the switchable photocurrent under the illumination of 570 nm, where photocurrent

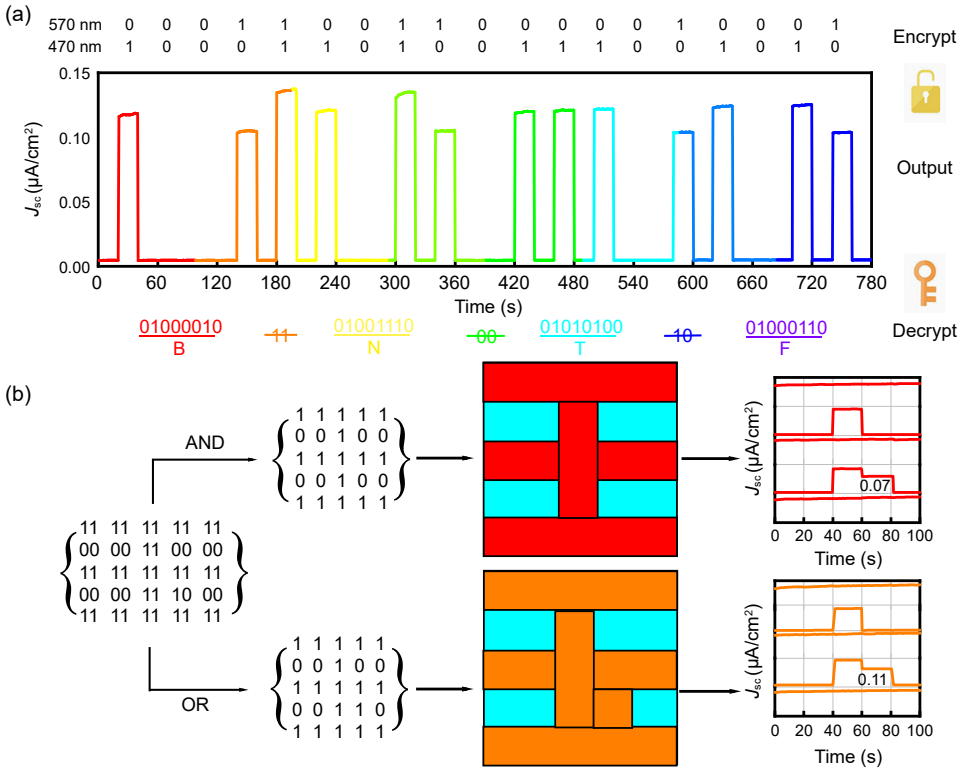

Fig. 5. (a) The encrypted communication "BNTF" based on ASCII codes. (b) The transmission image of Chinese characters.

has a linear dependence on the light irradiation power. The photocurrent switching between high- and low-level demonstrates excellent reproducibility and stability. The on/off ratio surpasses 10^3 in variable power density, which ensures the accuracy of weak signal detection. When exposed to 900 mW/cm^2 radiation, the $Bi_{0.5}Na_{0.5}Ti_{0.85}Fe_{0.15}O_3$ photodetectors present the on/off ratio of 10^5 in Fig. 4(a). The outstanding performance is verified in Table S1 of the SM, where the other multiferroic and heterojunction photodetectors are listed for comparison. Under stimulation (470 nm), the switchable photocurrent presents a similarly robust on/off ratio in Fig. 4(b). By mixed-light (470 nm and 570 nm) stimulation, the photocurrent reaches 0.16 μA/cm^2 in Fig. 4(c), which is ascribed to the spin transport network by the exchange interaction between local magnetic moments.[32]

The giant on/off ratio contributes to realizing the logic operations, and transforming information is modulated into four optical signal inputs by controlling the shut/open states of 470 nm and 570 nm light. A photocurrent intensity of 0.09 μA/cm^2 is used as the criterion in Fig. 4(d). When the light power density ranges from 514 to 642 mW/cm^2 and only open one light source (470 nm or 570 nm), the generated photocurrent is below 0.09 μA/cm^2. However, when both light simultaneously open, the photocurrent exceeds 0.09 μA/cm^2. When the incident light power exceeds 786 mW/cm^2, either a single light source or mixed light (470 nm and 570 nm) yields photocurrents exceeding 0.09 μA/cm^2. Thus, photocurrent values above the black dashed line are assigned "1", and those below are assigned "0". Aliovalent Fe substitution modifies the electronic structure and polarization intensity, which influences the separation and collection of photocarriers, realizing different logic outputs. Therefore, the switching states and power density of 470 nm and 570 nm lights sereve as optical-logic modulation to implement logic operations. The logic operations "AND" and "OR" are illustrated in Figs. 4(e) and 4(f), respectively. The stimulation is defined as follows: the condition of both lights can be "on" or "off", and light open is represented by "1", light shut is represented by "0". For example "10" indicates the single stimulation of 570 nm, and "01" means the stimulation of 470 nm. "11" indicates illumination with a mixed light source, "00" indicates no optical source. When the radiation power intensity is in the range of 514–642 mW/cm^2 and both lights are open, the photodetectors can implement the "AND" operation. When the light power exceeds 786 mW/cm^2, the photodetectors can showcase the "OR" operation.

The unique dual-band photoelectric response characteristics of $Bi_{0.5}Na_{0.5}Ti_{0.85}Fe_{0.15}O_3$ photodetectors enable optical encrypted communication. As shown in Fig. 5(a), the digital signals "00", "01", "10", and "11" are transmitted by the 470 nm and 570 nm light sources. Initially the encryption information "BNTF" was embedded into the digital data by assembling periodic effective signal segments using ASCII code, where the effective digital data is underlined in Fig. 5(a). According to the agreed-upon effective signal segments, the correct information of "BNTF" is decrypted by logic "AND" and "OR" operations, with the corresponding photocurrents serving as reference indexes to implement these logic operations. Therefore,

the dual-band-responsive $Bi_{0.5}Na_{0.5}Ti_{0.85}Fe_{0.15}O_3$ photodetectors possess in-sensor computing capability, where high-throughput data processing is reliable.

In order to demonstrate the practical sensor-computing application of $Bi_{0.5}Na_{0.5}Ti_{0.85}Fe_{0.15}O_3$ photodetectors, the transmission of a Chinese character is presented in Fig. 5(b). Using two individual light sources (470 nm and 570 nm), the light irradiation power of each wavelength is modulated to serve as the signal password input, while the corresponding photocurrent is recorded as the output signal. The Chinese character image is down-sampled into a 5×5 pixel matrix, and the corresponding codebook matrix is presented on the left in Fig. 5(b). Under stimulation of 470 nm and 570 nm mixed radiation, the encrypted image is decrypted through the characteristic photocurrent response. According to the previously defined photocurrent criterion, the "AND" and "OR" logic operations are switchable. When the "AND" logic value is "1", the corresponding effective pixel units turn red, while other elements display in blue. The Chinese character "王" is displayed within the 5×5 matrix. When the light power is further increased, the logic operation switches to the "OR" operation. The effective pixels turn orange when the "OR" logic value is "1", whereas the non-effective units remain blue. The previously transmitted Chinese character "王" transforms into "玉". If the encrypted signal is intercepted by unauthorized users, incorrect logical operations yield erroneous decryption images, ensuring secure and accurate information transmission.

In summary, Fe-doped $Bi_{0.5}Na_{0.5}Ti_{1-x}Fe_xO_3$ ($x = 0$, 0.05, 0.1, 0.15, 0.2, and 0.25) ceramic photodetectors were prepared by conventional solid-state sintering. Light-programmable logic operations are realized by the dual-band response (470 nm and 570 nm). The oxygen vacancy density and magnetic orders give rise to the dual-band response. The alphanumeric string "BNTF" is transmitted in ASCII format. Chinese characters "王" and "玉" are transmitted by "AND" and "OR" operations, respectively. These results highlight the application of multiferroic photodetectors in promising in-sensor computing and optical encrypted communication.

Data Availability Statement. The data that support the findings of this study are available upon reasonable request from the authors.

Acknowledgements. This work was supported by the National Natural Science Foundation of China (Grant Nos. 12564037, 12364037, and 12374258).

References

[1] Jang H, Lee J, Beak C, Biswas S, Lee S, and Kim H 2025 *Adv. Mater.* **37** 2416073
[2] Zhang Y Q, Ma Y, Wang Y X, Zhang X D, Zuo C T, Shen L, and Ding L M 2021 *Adv. Mater.* **33** 2006691
[3] Ma Z Z, Ji X Z, Lin S L, Chen X, Wu D, Li X J, Zhang Y, Shan C X, Shi Z F, and Fang X S 2023 *Adv. Mater.* **35** 2300731
[4] Gao Y, Zhao C, Pu K, He M, Cai W Q, Tang M C, Kang F Y, Yip H L, and Wei G D 2022 *Sci. Bull.* **67** 1982
[5] Su Y T, Zhen L, Song R M, Wu D, Zhao S F, and Bai Y L 2025 *J. Phys. Chem. Lett.* **16** 10506
[6] Han S G, Li M F, Liu Y, Guo W Q, Hong M C, Sun Z H, and Luo J H 2021 *Nat. Commun.* **12** 284
[7] Cao F, Yan T T, Li Z Q, Wu L M, and Fang X S 2022 *Adv. Opt. Mater.* **10** 2200786
[8] Ci W J, Wang P, Xue W H, Liu T Q, Qu J Y, and Xu X H 2025 *Adv. Funct. Mater.* **35** 2424926
[9] Wang Y Q, Liu R R, Ma T C, Wu Y B, Lu D Z, Zhang M H, Liang F, Yu H H Zhang H J, and Wu Y C 2025 *Nat. Commun.* **16** 8962
[10] Liu Y, Wang J L, Huang H L, Yun Y, Meng D C, Yang Q X, Zhai X F, Fu Z P, Knize R J, and Lu Y L 2017 *Adv. Opt. Mater.* **5** 1700158
[11] Huang W, Chakrabartty J, Harnagea C, Gedamu D, Ka I, Chaker M, Rosei F, and Nechache R 2018 *ACS Appl. Mater. Interfaces* **10** 12790
[12] Dolgikh A, Shapaeva T B, Yamada K T, Logunov M V, Rasing T H, and Kimel A V 2023 *Rev. Sci. Instrum.* **94** 103001
[13] Su Y T, Zhao S F, and Bai Y L 2025 *Appl. Phys.Lett.* **127** 122901
[14] Naderer M, Kainz T, Schütz D, and Reichmann K 2014 *J. Eur. Ceram. Soc.* **34** 663
[15] Harbi A, Azouaoui A, Benmokhtar S, and Moutaabbid M 2022 *J. Supercond. Nov. Magn.* **35** 1405
[16] Li Q, Zhang A H, Gao D, Guo M, Feng J J, Zeng M, Fan Z, Chen D Y, Gao X S, Zhou G F, Lu X B, and Liu J M 2019 *Appl. Phys. Lett.* **114** 202902
[17] Zhang M, Shi Y, Koval V, Yue Y J, Wu Z X, Wu Y Y, Zhou Y Q, Li T, Jia C L, and Yan H X 2025 *Phys. Rev. B* **112** 054423
[18] Chakraborty T, Ray S, and Itoh M 2011 *Phys. Rev. B* **83** 144407
[19] Jaiswar S and Mandal K D 2017 *J. Phys. Chem. C* **121** 19586
[20] Brovko O O and Tosatti E 2017 *Phys. Rev. Mater.* **1** 044405
[21] Rajamani A, Dionne G F, Bono D, and Ross C A 2005 *J. Appl. Phys.* **98** 063907
[22] Gouvea D 2024 *J. Eur. Ceram. Soc.* **44** 116677
[23] Yan H X, Inam F, Viola G, Ning H P, Zhang H T, Jiang Q H, Zeng T, Gao Z P, and Reece M J 2011 *J. Adv. Dielectr.* **1** 107
[24] Zeng F F, Zhang J J, Zhou C, Jiang L, Guo H T, Chen Y X, Lu W Z, Zhang H B, Cai W, Hu Y M, and Fan G F 2022 *ACS Sustainable Chem. Eng.* **10** 1277
[25] Peng P, Feng X, Chen T, Zhou R S, Xiao Q Q, Zhang L, and Zeng F F 2025 *Appl. Phys. Lett.* **127** 212901
[26] He R C, Guo H T, Yao Z K, Wang F P, Sun Q, Li X, Song X Q, Zhou R S, Xiao Q Q, Zhang L, Fan G F, Wang D W, Zeng F F, and Liu Q B 2025 *J. Adv. Ceram.* **14** 9221160
[27] Tang X Y, Hu Z M, Koval V, Baxter H, Eriksson M, Whiteley R, Banerjee K, Viola G, Yang B, and Yan H X 2025 *J. Materiomics* **11** 101052
[28] Shi X M, Wang J, Xu J W, Cheng X W, and Huang H B 2022 *Acta Mater.* **237** 118147
[29] O'Malley C J, Tang X Y, Koval V, Chen K, Wu Z X, Banerjee K, Hu W T, and Yan H X 2025 *J Adv. Ceram.* **14** 9221097
[30] Robertson I O, Whitefield B, Scholten S C, Singh P, Healey A J, Reineck P, Kianinia M, Barcza G, Ivády V, Broadway D A, Aharonovich I, and Tetienne J P 2025 *Nat. Phys.* **21** 1981
[31] Zhang C, Sun D, Sheng C X, Zhai Y X, Mielczarek K, Zakhidov A, and Vardeny Z V 2015 *Nat. Phys.* **11** 427
[32] Bai Q, Bao X X, He C Y, Wu D, Bai Y L, and Zhao S F 2024 *J. Phys. Chem. C* **128** 13763